LANGMUIR Article
Cite This: Langmuir 2017, 33, 13955−13963
pubs.acs.org/Langmuir

Position-Dependent Dynamics Explain Pore-Averaged Diffusion in Strongly Attractive Adsorptive Systems

William P. Krekelberg,*[,†] Daniel W. Siderius,[†] Vincent K. Shen,[†] Thomas M. Truskett,[‡] and Jeffrey R. Errington[§]

[†]Chemical Sciences Division, National Institute of Standards and Technology, Gaithersburg, Maryland 20899-8320, United States
[‡]McKetta Department of Chemical Engineering and Department of Physics, The University of Texas at Austin, Austin, Texas 78712, United States
[§]Department of Chemical and Biological Engineering, University at Buffalo, The State University of New York, Buffalo, New York 14260, United States

Supporting Information

ABSTRACT: Using molecular simulations, we investigate the relationship between the pore-averaged and position-dependent self-diffusivity of a fluid adsorbed in a strongly attractive pore as a function of loading. Previous work (Krekelberg, W. P.; Siderius, D. W.; Shen, V. K.; Truskett, T. M.; Errington, J. R. Connection between thermodynamics and dynamics of simple fluids in highly attractive pores. *Langmuir* **2013**, *29*, 14527−14535, doi: 10.1021/la4037327) established that pore-averaged self-diffusivity in the multilayer adsorption regime, where the fluid exhibits a dense film at the pore surface and a lower density interior pore region, is nearly constant as a function of loading. Here we show that this puzzling behavior can be understood in terms of how loading affects the fraction of particles that reside in the film and interior pore regions as well as their distinct dynamics. Specifically, the insensitivity of pore-averaged diffusivity to loading arises from the approximate cancellation of two factors: an increase in the fraction of particles in the higher diffusivity interior pore region with loading and a corresponding decrease in the particle diffusivity in that region. We also find that the position-dependent self-diffusivities scale with the position-dependent density. We present a model for predicting the pore-average self-diffusivity based on the position-dependent self-diffusivity, which captures the unusual characteristics of pore-averaged self-diffusivity in strongly attractive pores over several orders of magnitude.

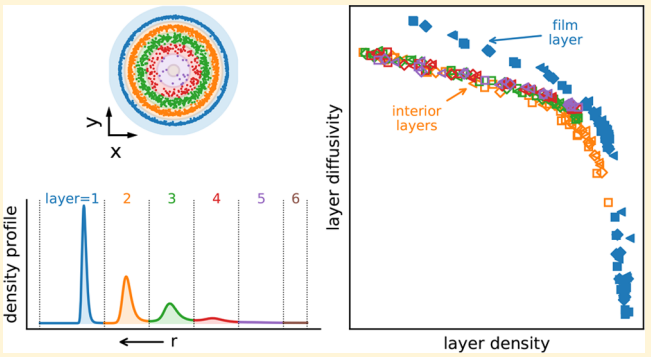

1. INTRODUCTION

Light gas adsorption in porous materials plays a vital role in a host of technologies such as carbon dioxide capture and natural gas storage.[1−5] One of the primary focuses in these applications is the adsorption capacity of the adsorbent for a given adsorbate. Consequently, considerable attention has been paid to the measurement and prediction of adsorption isotherms. Theory and simulation have been invaluable in connecting the adsorbent structure, adsorbent−adsorbate interactions, and confined-fluid structure to the resulting adsorption isotherms.[6−10]

Although equilibrium adsorption is one important consideration in applications involving porous materials, the dynamic properties of the (confined) adsorbate are also important. Although not as well understood as adsorption thermodynamics, these dynamic properties have recently received increased attention. For example, recent work has investigated the self-diffusivity in porous materials[11−13] and developed simplified molecular interpretations of intrapore transport using molecular simulations.[14−16] Other studies investigated Fickian transport diffusivity[17,18] and explored nonequilibrium adsorption hysteresis related to intrapore diffusion.[19,20] Theoretical studies examined the dynamics of pore filling, capillary condensation, cavitation, and pore-network effects using dynamic lattice fluid models[21−24] as well as developed models for Fickian- and self-diffusivity.[25,26] Considerable recent effort has been expended in modeling position-dependent self-diffusion in the strongly inhomogeneous direction normal to the pore boundaries.[27−30] Even with such studies, a reliable means to estimate the dynamic properties of a confined adsorbed fluid is lacking.

One promising approach for estimating the dynamic properties of adsorbed fluids is based on connecting such properties to well-understood thermodynamic characteristics. This was our focus in two recent studies.[31,32] Using exhaustive molecular simulation data, these studies showed that the self-

Received: September 28, 2017
Revised: November 6, 2017
Published: November 10, 2017

DOI: 10.1021/acs.langmuir.7b03401
Langmuir 2017, 33, 13955−13963

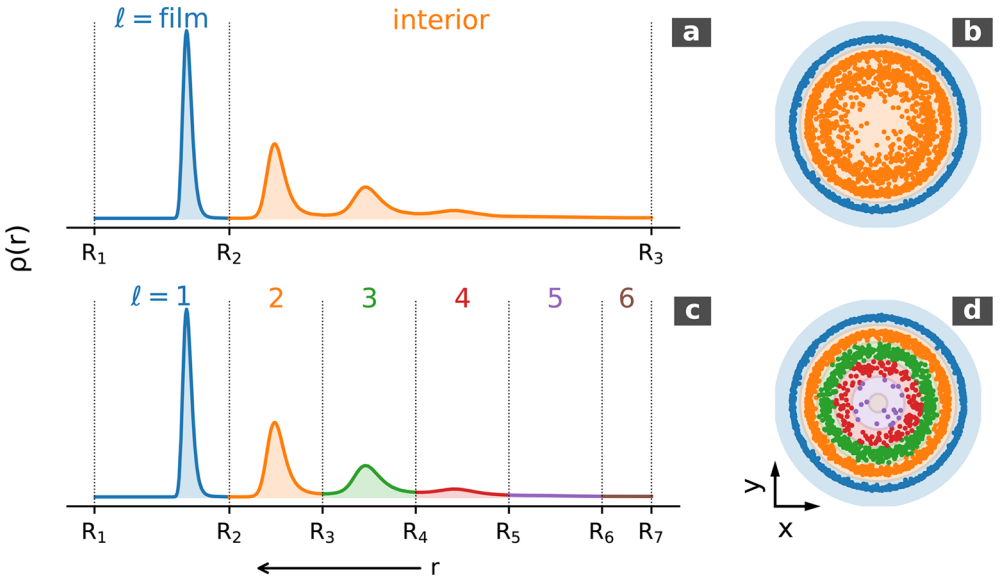

Figure 1. Representation of the (a, b) film−interior (FI) and (c, d) all-layer (ALL) partitioning schemes. (a, c) Layers in the resulting density profiles and (b, d) layers in snapshots taken from simulations.

diffusivity of a fluid adsorbed in a broad range of adsorbents can be linked to adsorption thermodynamics. In the case of weakly attractive adsorbents, the adsorbate self-diffusivity has the same scaling with fluid loading that the self-diffusivity of the bulk fluid has with density, allowing for the prediction of confined fluid self-diffusivity from pore loading and bulk data.[32] In the case of technologically important, strongly attractive adsorbents, such a simple link between dynamics and thermodynamics is not yet known to exist. However, strong qualitative links between adsorptive thermodynamics and the resulting dynamics have been observed in these systems.

Such strongly attractive systems display three distinct adsorptive regimes, each of which can be directly tied to the structure of the adsorbed fluid.[31] At low pressure and fluid loading, fluid particles are located adjacent to the pore surface as a result of the strong fluid−solid attraction, leading to the formation of a single, well-defined fluid film. Accordingly, this is referred to as the film (or monolayer) formation regime. In this regime, the pore-averaged axial self-diffusivity, D_{tot}, of the confined fluid decreases exponentially with loading. At moderate pressure and loading, fluid particles begin to occupy interior portions of the pore (i.e., interior to the film layer), and this is referred to as the multilayer adsorption regime. In this regime, D_{tot} is approximately constant as a function of pore loading, which is driven by increasing reservoir pressure, and remains nearly constant. Finally, at high pressure and loading, fluid particles occupy the entire pore, and increasing pressure leads to the densification of fluid layers. This is referred to as the pore-filling regime. In this regime, D_{tot} (again) decreases with loading.

Given our general expectation that the self-diffusivity should decrease as the amount of fluid in the pore increases, the nearly constant value of D_{tot} in the multilayer adsorption regime is a surprising finding. What leads to the constant self-diffusivity in the multilayer adsorption regime, where fluid loading and underlying fluid structure vary by a large degree, is an open question. It was also observed[31] in the film-formation regime at subcritical temperatures that D_{tot} is directly linked to the density of the film layer. This suggests the possibility that for interior fluid layers, the dynamics in a layer connect to fluid structure within that layer. It also suggests a possible explanation of the constant value of D_{tot} in the multilayer adsorption regime. Specifically, we hypothesized that the constant value of D_{tot} in the multilayer adsorption regime is the result of the simultaneous addition of slow particles in the dense film layer and fast particles in the less dense interior portions of the pore.

In this article, we investigate the position-dependent dynamics of a fluid adsorbed in strongly attractive pores using molecular simulations. The fluid and adsorbent models were chosen to mimic a realistic adsorbate−adsorbent system that might be encountered in practice. We use our simulation results to address two specific questions: What leads to the nearly constant pore-averaged axial self-diffusivity as a function of loading in the multilayer adsorption regime, and do position-dependent dynamics scale with local density under these conditions? The article is organized as follows. Section 2 discusses the simulation methods and fluid and solid models used. Section 3 presents our simulation results and discusses the connection between position-dependent dynamics and pore-averaged dynamics. Section 4 summarizes our main findings.

2. THEORETICAL METHODS

2.1. Simulation Methods. We used the same model and simulation methods as in ref 31. In brief, we simulated argon in a single cylindrical, multiwalled carbon nanotube (CNT) using molecular dynamics in the canonical ensemble with N = 4000 particles. The argon fluid was modeled with the Lennard-Jones potential with particle size parameter σ and energy parameter ϵ. The potential was truncated with a linear force shift at cutoff distance r_{cut} = 2.5σ. The CNT adsorbent was modeled with a cylindrical Steele 10-4-3 potential[33] with pore radius parameter R.

The geometry of the simulation cell was set to $2R \times 2R \times L_z$, where L_z, the length of the pore in the axial and periodically replicated z dimension, was varied to achieve the desired pore-averaged fluid density (or loading) $\rho = N/(\pi R^2 L_z)$. We investigated pores of size R/σ = 5.98, 7.77, and 11.56 at reduced temperatures k_BT/ϵ = 0.73, 0.85, and 1.5. Because the bulk critical temperature of the fluid is k_BT_c/ϵ = 0.93,[34] we refer to k_BT/ϵ = 1.5 as supercritical and k_BT/ϵ = 0.73 and 0.85 as subcritical. Self-diffusion data for the bulk fluid and confined

DOI: 10.1021/acs.langmuir.7b03401
Langmuir 2017, 33, 13955−13963

fluid at $R/\sigma = 3.99$ and 8.97 and the above temperatures were taken directly from ref 31.

2.2. Position-Dependent Dynamics. Position-dependent dynamics were calculated using the method detailed in ref 35. The system was partitioned into N_P cylindrical shells, labeled as $l = 1, 2,..., N_P$ with boundaries $R = R_1 > R_2 >...> R_{N_P} > R_{N_P+1} = 0$. A particle is in partition l if its radial position $r = \sqrt{x^2 + y^2}$ satisfies $R_l > r \geq R_{l+1}$. Therefore, $l = 1$ is the partition closest to the solid surface, and $l = N_P$ is the partition closest to the center of the pore. Note that these partitions are simply part of a bookkeeping strategy.

We investigated two partitioning schemes, both of which are defined in terms of the fluid layers formed within a CNT pore. The first divides the system into a film (F) partition encompassing the fluid layer closest to the solid surface and an interior (I) partition encompassing everything else. We term this the film−interior (FI) partitioning. The second divides the system into all distinguishable fluid layers in the pore. We term this the all-layers (ALL) partitioning. When discussing the film−interior partitioning, we refer to partitions explicitly as film (F) and interior (I). When discussing the all-layers partitioning, we refer to partitions by index $l \in [1, N_L]$. Note that, as defined, the $l = 1$ partition in the ALL scheme is identical to the film partition in the FI scheme.

The boundaries between partitions $R_{l\geq 2}$ were chosen to correspond to the boundaries between fluid layers, defined by local minima in the density profile. We found (Supporting Information Figures S-1 and S-2) that the locations of the minima are approximately captured by the relationship $R_{l\geq 2} = R - (l - 0.55)\sigma$. Figure 1a,b displays the film−interior partitioning, and Figure 1c,d displays the all-layer partitioning. As defined, a majority of individual partitions we investigated (the film partition in the FI scheme and all the partitions in the ALL scheme) correspond to visually confirmed fluid layers, and we will therefore sometimes refer to such partitions as layers. The one exception to this is the interior partition in the FI scheme, which we always refer to as the interior partition.

The self-diffusivity in the axial direction z in a partition l was calculated as follows.[35] Over the time interval $[t_0, t_0 + t]$, let $S_l(t_0, t_0 + t)$ denote the set of particles that stay in l over the entire interval, let $N_l(t_0, t_0 + t)$ denote the number of such particles, and let $N_l(t_0)$ denote the number of particles in the partition at the beginning of the time interval. The mean-squared displacement in the z direction in partition l is defined as

$$\langle \Delta z^2(t) \rangle_l \equiv \left\langle \frac{1}{N_l(t_0)} \sum_{i \in S_l(t_0, t_0+t)} [z_i(t_0 + t) - z_i(t_0)]^2 \right\rangle_{t_0} \quad (1)$$

where $\langle \cdot \rangle_{t_0}$ indicates an average over time origin t_0. The self-diffusivity in the axial direction z in partition l is then defined as[35]

$$D_l \equiv \lim_{t \to \infty} \frac{\langle \Delta z^2(t) \rangle_l}{2tP_l(t)} \quad (2)$$

where $P_l(t) \equiv \langle N_l(t_0, t_0 + t)/N_l(t_0) \rangle_{t_0}$ is the survival probability in partition l. The pore-averaged self-diffusivity in the axial direction z, denoted by D_{tot}, was calculated from the total mean-squared displacement. This is equivalent to a partition self-diffusivity if the pore is divided into a single partition with $R_1 = R$ and $R_2 = 0$. In this study, we considered only diffusivity in the axial direction and therefore drop the explicit reference to z.

We will make reference to the term partition-averaged self-diffusivity, defined as the molar average of D_l over all partitions for a given partitioning scheme:

$$\bar{D}_P \equiv \sum_{l \in P} x_l D_l \quad (3)$$

where $P \in \{FI, ALL\}$ indicates the partitioning scheme and x_l is the fraction of fluid particles in partition l. For a given partition l, the number of particles in the partition is $N_l = \int_{R_{l+1}}^{R_l} 2\pi r L_z \, dr \, \rho(r)$, where $\rho(r)$ is the radial density profile and $x_l = N_l/N$.

Although not exhaustively studied, we analyzed the errors in diffusivities by considering each time origin (eq 1) to be an independent estimate. We found that in almost all cases the uncertainty in the pore-averaged and partition-dependent self-diffusivities is smaller than the symbol size used in Figures 3−6.

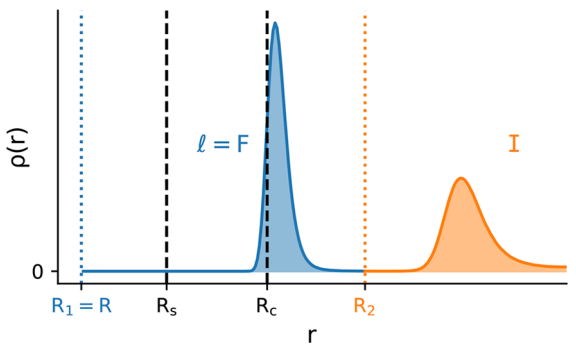

Figure 2. Representation of the different values used in the determination of the film volume. The effective center-accessible radial dimension R_c is equal to the Barker−Henderson pore size R_{BH}, and the surface-accessible radial dimension is $R_s = R_c + \sigma_{BH}/2$.

2.3. Partition Density and Effective Geometric Parameters. We also require measures of the density within partitions. The density of particles in partition l is defined by $\rho_l \equiv N_l/V_l$, where V_l is the volume measure of partition l. For interior partitions ($l \geq 2$), the volume is defined as the total partition volume given by $V_{l\geq 2} = \pi L_z(R_l^2 - R_{l+1}^2)$. For the film partition, we investigate two volume measures—one based on the center-accessible volume and the other based on the surface-accessible volume—that differ only in the choice of the upper bound of the radial dimension. As discussed in ref 32, parameter R used in the fluid−solid potential is not strictly equal to the radial positions accessible to fluid particles. Instead, we consider the upper bound in terms of the Barker−Henderson[32,36] pore size R_{BH}, which is effectively the radial dimension of the pore accessible to particle centers. Note that R_{BH} is implicitly a function of both temperature and fluid−solid interaction. Therefore, we define the center accessible radial dimension by $R_c = R_{BH}$ and the center-accessible film volume by $V_{F,c} \equiv \pi L_z(R_c^2 - R_2^2)$. The radial dimension accessible to particle surfaces is similarly defined as $R_s = R_c + \sigma_{BH}/2$, where σ_{BH} is the Barker−Henderson particle diameter[36] and the surface-accessible film volume is defined by $V_{F,s} \equiv \pi L_z(R_s^2 - R_2^2)$. We denote the film density as $\rho_{F,x}$, where $x \in \{c, s\}$ denotes either the center- or surface-accessible volume, respectively. Figure 2 displays locations R_c and R_s at a single state point. We emphasize that R_c and R_s are used only in the calculation of the volume measure.

When comparing results at different pore sizes and temperatures, it is more meaningful to compare them in terms of length and times scales based on the Barker−Henderson diameter and pore size. That is, length is normalized by σ_{BH}, and time is normalized by $\sqrt{\sigma_{BH}^2 m/(k_B T)}$. For notational convenience and clarity, such quantities will be marked with a superscript (*). For example, $D_l^* = D_l(k_B T \sigma_{BH}^2/m)^{-1/2}$, and $\rho_l^* = \rho_l \sigma_{BH}^3$. We also make reference to the effective surface-accessible pore density[32] (or effective loading), defined as $\rho_s^* = N\sigma_{BH}^3/(\pi R_s^2 L_z)$, where R_s is the effective surface-accessible radial pore dimension defined above.

3. RESULTS AND DISCUSSION

3.1. Decomposing Pore-Averaged Self-Diffusivity. We begin by investigating the position-dependent dynamics of a fluid in a pore of size $R/\sigma = 5.98$ when the system is divided

DOI: 10.1021/acs.langmuir.7b03401
Langmuir 2017, 33, 13955−13963

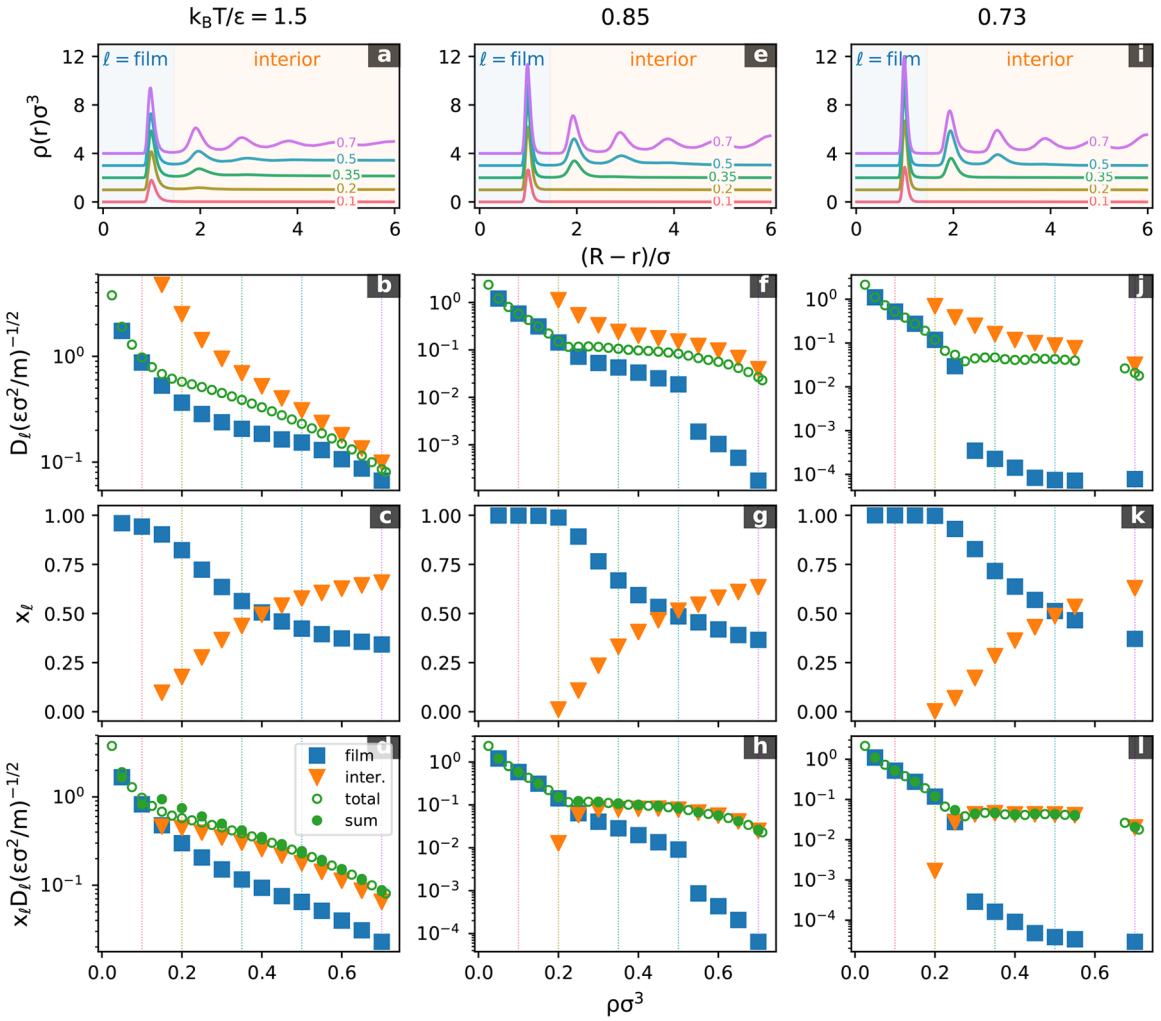

Figure 3. Properties of the argon fluid in a CNT pore of size R/σ = 5.98 at temperatures $k_BT/\in$ = 1.5, 0.85, and 0.73 indicated at the top of each column. (a, e, i) Density profiles at indicated pore loadings of $\rho\sigma^3$. (b, f, j) Film, interior, and pore-averaged self-diffusivities. (c, g, k) Mole fraction of particles in film and interior partitions. (d, h, l) Contribution to total diffusion x_lD_l, sum of contributions $\sum x_lD_l$ (i.e., the partition averaged self-diffusivity defined in eq 3), and pore-averaged self-diffusivity D_{tot}.

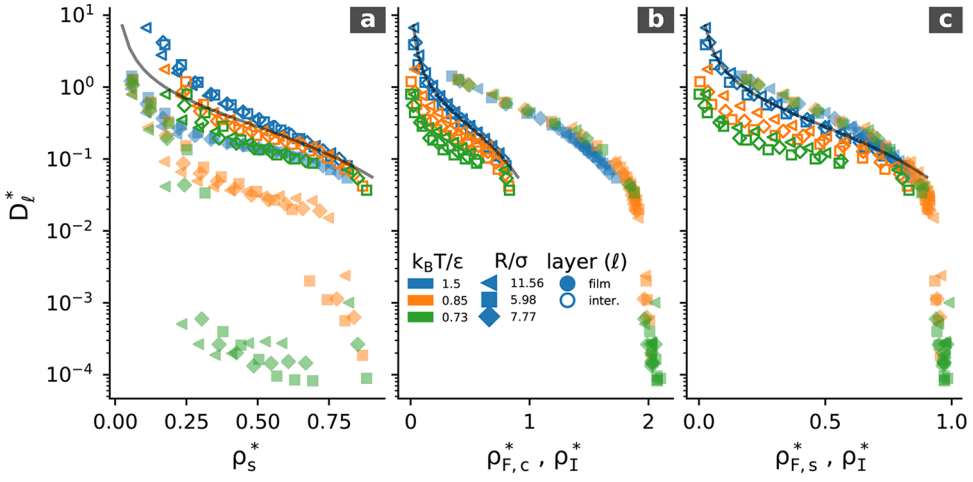

Figure 4. Position-dependent self-diffusivity with the film−interior partitioning scheme versus density measure: (a) total effective surface-accessible density ρ^*_s, (b) effective center-accessible film and total interior density, and (c) effective surface accessible film and total interior density. The solid lines in (a−c) are the bulk diffusivity (D^*_{bulk}) vs bulk density (ρ^*_{bulk}) at $k_BT/\in$ = 1.5. Note that the quantities are normalized as discussed in section 2.3.

DOI: 10.1021/acs.langmuir.7b03401
Langmuir 2017, 33, 13955−13963

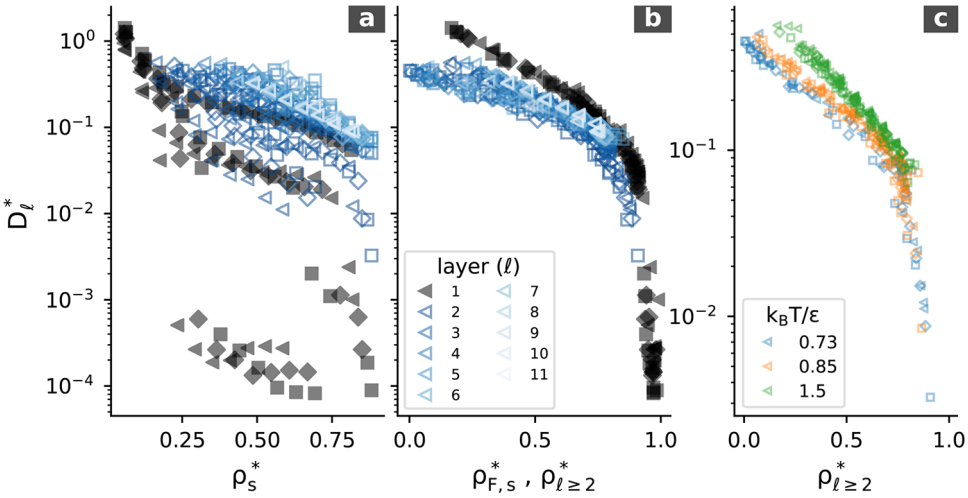

Figure 5. Position-dependent self-diffusivities using the all-layer partitioning scheme versus (a) total effective density and (b, c) layer density. Colors correspond to the layer index in (a, b) and temperature in (c).

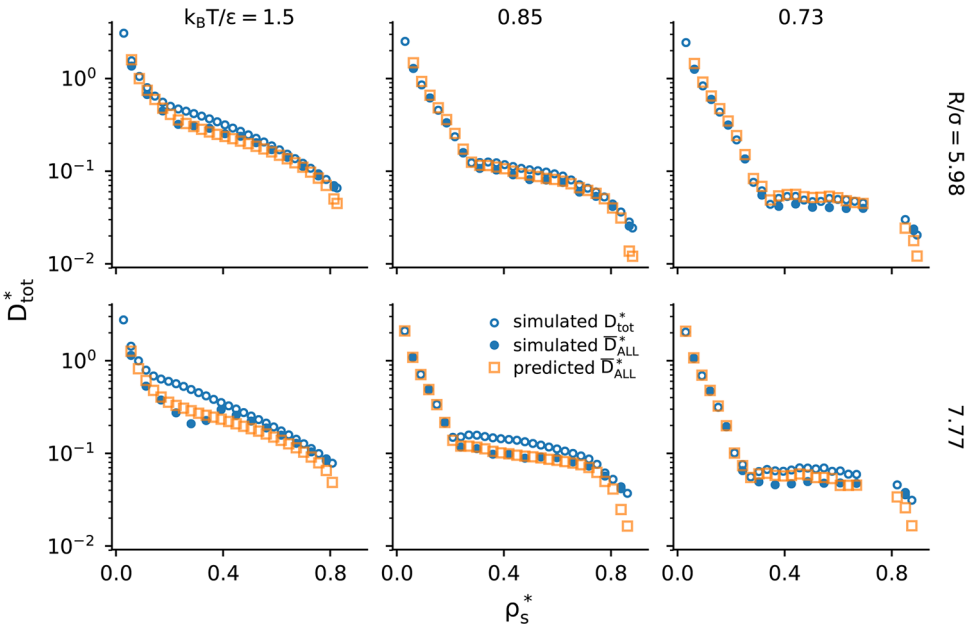

Figure 6. Comparison of the pore-averaged self-diffusivity D^*_{tot} from simulation, the ALL-based partition-averaged self-diffusivity $\overline{D}^*_{ALL}$ from simulation, and the model prediction to the ALL-based partition-averaged self-diffusivity and the prediction from eq 4.

into a film partition and a single interior partition, i.e., the film−interior (FI) partitioning scheme described above, at the supercritical temperature $k_BT/\epsilon = 1.5$. For reference, Figure 3a displays the density profiles $\rho(r)$ at several pore loadings ρ. Figure 3b displays the self-diffusivity in the film (D_F) and the interior (D_I) partitions, as well as the pore-averaged self-diffusivity D_{tot}. All self-diffusivities decrease monotonically with increasing pore loading. At low loading ($\rho\sigma^3 < 0.1$), the average self-diffusivity is nearly identical to the film self-diffusivity, $D_{tot} \approx D_F$, and at higher loading, we observe that $D_F < D_{tot}$. The self-diffusivity in the interior partition is always greater than the pore-averaged diffusivity.

These observations are easily explained in terms of the confined fluid structure. For reference, Figure 3c displays the fraction of particles in the film and interior partitions as a function of loading at $k_BT/\epsilon = 1.5$. At low loading, $x_F \approx 1$, and it follows that D_F is very similar to D_{tot}. For $\rho\sigma^3 \gtrsim 0.15$, particles begin to occupy interior potions of the pore away from the solid−pore surface, but the maxima in the density profiles are much higher in the film layer than in any of the interior layers. Therefore, we expect $D_I > D_F$ because particles located in the interior partition are less frustrated than they are in the film layer. Because D_{tot} is composed of contributions from the entire pore, we expect D_{tot} to be bounded below by D_F and bounded above by D_I (i.e., $D_F < D_{tot} < D_I$).

Figure 3j displays the self-diffusivities at the subcritical temperature $k_BT/\epsilon = 0.73$. Note that at this temperature, D_{tot} exhibits the three diffusivity regimes discussed previously.[31] Of particular interest, at moderate densities ($0.225 \leq \rho\sigma^3 \leq 0.55$), D_{tot} is nearly constant with respect to loading. Consistent with the results at the supercritical temperature, D_{tot} is very similar to D_F at low loading at this subcritical temperature. In fact, $x_F = 1$ for $\rho\sigma^3 \leq 0.2$ (Figure 3k), so it follows that $D_{tot} = D_F$ under these conditions, which Figure 3j shows. We again observe that $D_F < D_{tot} < D_I$. However, for $\rho\sigma^3 \geq 0.25$, note that whereas D_I is comparable at $k_BT/\epsilon = 1.5$ and 0.73, D_F is significantly lower

DOI: 10.1021/acs.langmuir.7b03401
Langmuir 2017, 33, 13955−13963

at $k_BT/\epsilon = 0.73$ than at the supercritical temperature. This decreased mobility is reflected by the increased peak height in the film layer at the lower temperature $k_BT/\epsilon = 0.73$ (compare Figure 3a,i and see also Supporting Information Figure s-3), which is an indication of increased frustration. At both temperatures, D_I decreases moderately with increasing loading. (Note that we more closely compare the position-dependent dynamics across temperatures below.) It is interesting that for $\rho\sigma^3 \gtrsim 0.4$, D_F is nearly constant. This is due to the film layer becoming saturated and not changing appreciably for loadings beyond $\rho\sigma^3 \gtrsim 0.4$ (Supporting Information Figure S-3). We note that both D_F and D_I behave in a qualitatively normal manner, by which we mean that self-diffusivities decrease with increasing fluid loading.

Figure 3f displays the self-diffusivities at the moderately subcritical temperature $k_BT/\epsilon = 0.85$. At this temperature, D_{tot} still displays the three distinct diffusivity regimes. D_{tot} is nearly constant at moderate loading, decreasing only slightly with loading. Still, the behavior at moderate loading is clearly distinguishable from that at low loading. Again, $D_{tot} = D_F$ at low loading, and $D_F < D_{tot} < D_I$ holds. The primary difference between the two subcritical temperatures is that D_F is larger at the higher temperature, which is due to the tendency of the film layer density to decrease with increasing temperature (Supporting Information Figure S-3). The behavior of D_I is similar at the two subcritical temperatures.

We now address whether the pore-averaged self-diffusivity D_{tot} can be quantitatively linked to the partition-averaged self-diffusivity $\bar{D}_{FI}$, defined in eq 3. We note that, in general, these quantities do not have to be equal. The partition-averaged self-diffusivity depends on the partitioning scheme used. Also, the pore-average self-diffusivity includes trajectories that pass between multiple layers, and the partition-averaged self-diffusivity includes only trajectories that remain entirely within a given partition. Still, if one chooses the partitioning appropriately and if the self-diffusion in the radial direction is negligible, then we expect that D_{tot} will be at least approximately equal to $\bar{D}_{FI}$.

Figure 3d,h,l compares the partition-averaged diffusivity $\bar{D}_{FI}$ to the pore-averaged self-diffusivity D_{tot}. At subcritical temperatures, D_{tot} is indistinguishable from $\bar{D}_{FI}$. However, at the supercritical temperatures, there are differences, especially at moderate loadings. This is not surprising because we expect radial diffusion to increase with temperature. Thus, $\bar{D}_{FI}$ will not include trajectories that cross layers in a diffusive time τ. Still, even with this difference, we see that $\bar{D}_{FI}$ describes D_{tot}, at worst semiquantitatively.

Therefore, we can decompose D_{tot} into film and interior contributions. Figure 3d,h,l displays contributions x_lD_l for the film and interior partitions to $\bar{D}_{FI}$. As expected, the pore-averaged self-diffusivity at low loading is completely described by film contribution x_FD_F. Interestingly, at the subcritical temperature $k_BT/\epsilon = 0.73$ for $\rho\sigma^3 \gtrsim 0.25$, D_{tot} is completely described by the contribution from the interior partition x_ID_I. It follows that $x_FD_F \ll x_ID_I$. In fact, we observe that the film contribution is approximately 3 orders of magnitude less than the interior contribution. Therefore, the constant value of D_{tot} at subcritical temperatures and moderate densities is due to the cancellation of two effects that take place with increasing pore loading, namely, the simultaneous increase in x_I and decrease in D_I.

It is now interesting to investigate the higher, but still subcritical, temperature $k_BT/\epsilon = 0.85$. First, note that x_ID_I is very similar at the two subcritical temperatures. However, as discussed above, D_F is much higher at $k_BT/\epsilon = 0.85$ than at 0.73; therefore, x_FD_F is non-negligible at this temperature. Therefore, the very slight decrease in D_{tot} at moderate densities and $k_BT/\epsilon = 0.85$ is due to the increased self-diffusivity in the film layer in comparison to the lower temperature.

The other pore sizes investigated (Supporting Information Figures S-5 and S-6) display qualitatively identical results to those presented here. We have also performed an identical analysis using the all-layer partitioning scheme (Supporting Information Figures S-7–S-9). The analysis of this partitioning is more complicated as a result of the larger number of distinct interior layers. Nonetheless, the partition-averaged self-diffusivity $\bar{D}_{ALL}$ still captures the characteristics of D_{tot}, although $\bar{D}_{ALL}$ tends to underestimate D_{tot} at supercritical temperatures and at subcritical temperatures in large pores. This is expected because radial self-diffusivity will play an increasing role in these cases.

3.2. Position-Dependent Dynamics and Local Density.

We now turn to a more detailed investigation of how position-dependent self-diffusivity relates to the position-dependent structure. This is motivated by the previously discussed observation that pore-averaged self-diffusivity in the film-formation regime scales with film density.[31] Given the above observation that $D_F \approx D_{tot}$ at low loading, this suggests that the D_F itself scales with film density. This in turn suggests the possibility that position-dependent self-diffusivities throughout the pore might scale with local density.

The FI-based position-dependent self-diffusivities are displayed as a function of loading in Figure 4a at all temperatures and pore sizes considered in this work. Here, we present data in terms of the Barker–Henderson normalized quantities (section 2.3). We first make some observations mentioned previously more precise. At moderate effective surface-accessible loading ρ_s^*, we clearly see a large variation in D_F^* with temperature, with $D_F^*(k_BT/\epsilon = 0.73)$ being much lower than the other two temperatures considered. We also see that the variability of D_I^* is very small in comparison to that of D_F^*.

We next consider the position-dependent self-diffusivities in terms of the local density. Figure 4b displays D_F^* as a function of center-accessible film density $\rho_{F,c}$, and D_I^* as a function of ρ_I^* (section 2.3). We note that this definition of the film density is similar to that used in ref 31. There, it was observed that D_{tot} in the film-formation regime at subcritical temperatures scales as a single universal function of film density. It was also observed in the film-formation regime at supercritical temperatures that D_{tot} scaled with film density, although with a relationship that differed from the subcritical one. However, we see here that that D_F^* is a single function of $\rho_{F,c}^*$ regardless of temperature or pore size. Given the large differences in D_F^* with temperature noted above, this universal scaling is surprising. On the other hand, D_I^* is clearly not a universal function of ρ_I^*, a point we will return to shortly. In Figure 4b, we see that $D_F^* \to 0$ at $\rho_{F,c}^* \approx 2$ whereas $D_I^* \to 0$ at $\rho_I^* \approx 1$. That is, the scale of the position-dependent self-diffusivities is very different for these two density measures. Recall that $\rho_{F,c}^*$ considers the center-accessible volume. If we instead consider D_F^* in terms of the surface-accessible film density $\rho_{F,s}^*$, as shown in Figure 4c, then we see that the scales for D_F^* and D_I^* and even D_{bulk}^* are similar. Although $\rho_{F,s}^*$ shifts the divergence of D_F^*, it has no effect on the universal scaling. That is, D_F^* remains a universal function of $\rho_{F,s}^*$.

DOI: 10.1021/acs.langmuir.7b03401
Langmuir 2017, 33, 13955–13963

As an aside, it has been shown for a variety of fluids that the total pore-averaged self-diffusivity is a nearly univeral function of the surface-accessible density but not a universal function of the center-accessible density.[37] This suggests that the surface-accessible definition of film density is more relevant to diffusivity than a definition based on the center-accessible volume.

Figure 4c also shows more clearly the variability of D_I^*. At a fixed value of ρ_I^*, D_I^* decreases with decreasing temperature and decreasing pore size. However, it appears that the dependence on temperature is greater than the dependence on pore size. Interestingly, at $k_BT/\epsilon = 1.5$, D_I^* has the same dependence on ρ_I^* that the scaled bulk self-diffusivity has on the scaled bulk density, suggesting at supercritical temperatures that the interior of the pore is similar to the bulk fluid. (Note that in reduced form the bulk self-diffusivity is a universal function of density, which is shown in Supporting Information Figure S-4.) This is consistent with the fact that structuring in the interior layers is less pronounced at supercritical temperatures than at subcritical temperatures (compare Figure 3a to Figure 3e,i.)

Of course, that D_I^* does not scale universally with interior density is not surprising. The interior partition is composed of several fluid layers whose properties depend strongly on both temperature and pore size. We therefore next investigate how the self-diffusivities of each fluid layer D_l^*, as determined using the all-layers partitioning scheme, scale with local density ρ_l^*. Figure 5a displays D_l^* as a function of loading for all temperatures and pore sizes considered. Because the $l = 1$ layer is exactly equivalent to the film layer discussed above, we discuss only the interior layers $l \geq 2$. As a function of effective surface-accessible loading ρ_s^*, $D_{l\geq 2}^*$ displays wide variability as a function of l, temperature, and pore size. If we instead consider $D_{l\geq 2}^*$ as a function of layer density $\rho_{l\geq 2}^*$, as shown in Figure 5b, we see that $D_{l\geq 2}^*$ scales at least approximately with $\rho_{l\geq 2}^*$. More specifically, consider the temperature dependence of $D_{l\geq 2}^*(\rho_{l\geq 2}^*)$, shown in Figure 5c. We see two groupings of the data at low layer density, one for supercritical and one for subcritical temperatures. However, the variability observed in $D_I^*(\rho_I^*)$ with pore size does not exist for $D_{l\geq 2}^*(\rho_{l\geq 2}^*)$.

3.3. Model for Pore-Averaged Self-Diffusion. The above observations regarding the position-dependent self-diffusivities provide the basis for a simple model for the pore-averaged self-diffusivity D_{tot}^*. Specifically, given an estimator for $D_l^*(\rho_l^*)$ for a partitioning scheme P, we can make the approximation

$$D_{tot}(\rho, T, R)^* \approx \bar{D}_P^*(\rho, T, R) = \sum_{l\in P} x_l D_l^*(\rho_l^*) \tag{4}$$

where quantities x_l and ρ_l^* depend only on the static density profile $\rho(r; \rho, T, R)$ within the pore that could, for example, be calculated by Monte Carlo simulations or statistical mechanical density-functional theory.

We cannot provide a model for $D_l^*(\rho_l^*)$ based on first principles. Instead, we view eq 4 as a means, based upon a single series of measurements, to estimate pore-averaged self-diffusivity over a range of different conditions (e.g., loading, temperature, and pore size). Although D_{tot} is well approximated by $\bar{D}_{FI}$ (and hence $D_{tot}^* \approx \bar{D}_{FI}^*$), D_I^* is not a universal function of ρ_I^*. On the other hand, D_{tot}^* is at least semiquantitatively described in terms of $\bar{D}_{ALL}^*$ (Supporting Information Figures S-7−S-9). Additionally, both $D_I^* = D_F^*$ and $D_{l\geq 2}^*$ are approximately universal functions of layer density. We therefore build our model around the all-layer partitioning.

For example, we choose as a reference our simulation data at the state point $R/\sigma = 7.77$ and $k_BT/\epsilon = 0.85$. We calculate the position-dependent self-diffusivities at other state points by interpolating the reference data according to

$$\begin{aligned} D_1^*(\rho_{1,s}^*) &= D_1^{*,\mathrm{ref}}(\rho_{1,s}^*) \\ D_{l\geq 2}^*(\rho_{l\geq 2}^*) &= D_2^{*,\mathrm{ref}}(\rho_{l\geq 2}^*) \end{aligned} \tag{5}$$

where superscript ^{ref} denotes the reference data. Note that the estimator for $l \geq 2$ is based on the reference data in the $l = 2$ layer only. That is, we have utilized the fact that interior layers follow an approximately universal scaling (Figure 5). Therefore, our model is given by

$$\begin{aligned} D_{tot}^*(\rho, T, R) &\approx \bar{D}_{ALL}^*(\rho, T, R) \\ &\approx \bar{D}_{ALL}^{*,\mathrm{pred}}(\rho, T, R) \\ &\equiv x_1 D_1^{*,\mathrm{ref}}(\rho_{1,s}^*) + \sum_{l\geq 2} x_l D_2^{*,\mathrm{ref}}(\rho_l^*) \end{aligned} \tag{6}$$

where the last line defines our model prediction of the partition-averaged self-diffusivity $\bar{D}_{ALL}^{*,pred}$ based on the reference dynamic data at $k_BT/\epsilon = 0.85$ and $R/\sigma = 7.77$. Substituting values of x_l and ρ_l^* at a given combination of ρ, T, and R from our simulation data into the last line of eq 6 leads to our predicted pore-averaged self-diffusivities.

Figure 6 compares the values of D_{tot}^*, $\bar{D}_{ALL}^*$, and $\bar{D}_{ALL}^{*,pred}$ at pore sizes $R/\sigma = 5.98$ and 7.77. Comparisons at additional pore sizes are shown in Supporting Information Figure S-10. First, note that $\bar{D}_{ALL}^{*,pred}$ captures the behavior of $\bar{D}_{ALL}^*$ very well, especially at the reference state of $k_BT/\epsilon = 0.85$ and $R/\sigma = 7.77$. The estimates at other state points are, at worst, semiquantitative. This verifies that the self-diffusivity in the first two layers at a single state point can be used to extrapolate the partition-averaged self-diffusivity to other state points accurately.

The prediction of D_{tot}^* based on eq 6 depends on the approximation $D_{tot}^* \approx \bar{D}_{ALL}^*$. As discussed above, the ALL-based partition-averaged self-diffusivity captures the behavior of D_{tot} approximately, although it tends to underestimate D_{tot} at supercritical temperatures and at subcritical temperatures in large pores as a result of the increased radial self-diffusivity in these cases. Therefore, the model in eq 6 predicts the pore-averaged self-diffusivity well at subcritical temperatures and moderate pore sizes. However, given that D_{tot} spans more than 2 orders of magnitude, the prediction based on eq 6 is impressive.

4. CONCLUSIONS

We have investigated how the pore-averaged self-diffusivity in strongly attractive pores relates to position-dependent dynamics using molecular simulations. We found that the pore-averaged self-diffusivity can be decomposed into distinct contributions from fluid particles in the film layer and the pore interior. This observation allowed us to identify the microscopic origins of self-diffusivity characteristics in strongly attractive pores. Specifically, we found that the constant pore-

DOI: 10.1021/acs.langmuir.7b03401
Langmuir 2017, 33, 13955−13963

averaged self-diffusivity observed in the multilayer adsorption regime as a function of loading is linked to the constant self-diffusivity contribution of fluid in the interior of the pore. This contribution is insensitive to pore loading and arises from the cancellation of two effects. The first is the increase in the fraction of particles occupying the interior of the pore, and the second is the decrease in mobility due to the corresponding increase in fluid density (or frustration) in the interior of the pore. We also found that the self-diffusivities in individual fluid layers scale with the fluid density within each layer (with an appropriate definition of layer volume). These observations provide the basis of a model to estimate the pore-averaged self-diffusivity based on the fraction of fluid in a layer and density of fluid in a layer, both of which depend only on the static density profile, as well as limited layer dependent self-diffusivity data. This model captures the important characteristics of the pore-averaged self-diffusivity in strongly attractive pores at subcritical temperatures spanning more than 2 orders of magnitude.

This work leads to several questions for future research to address. One important question is the impact of fluid−solid interactions on the position-dependent dynamics. It was previously shown[32] that the pore-averaged self-diffusivity in weakly attractive adsorbents is fundamentally different than in strongly attractive adsorbents. For weakly attractive systems, does the scaling of position-dependent dynamics with local density hold, and if so, is the scaling similar to that observed here? We speculate that because the film layer in weakly attractive systems is less dense than in the strongly attractive system studied here, perhaps the self-diffusivities in the film and interior layers have similar scalings with layer densities in weakly attractive systems as opposed to the separate scaling observed here in a strongly attractive system. Also of interest is how the partitioning scheme impacts the analysis presented here. If the partitions are made infinitesimally small, then eq 4 is invalid because the self-diffusivity in the radial direction is not negligible and the pore-averaged self-diffusivity is instead linked to the partition self-diffusivities through a stochastic partial differential equation.[27] Still, an analysis with infinitesimally small partitions may show interesting self-diffusivity characteristics within individual layers. We also emphasize that the analysis presented here pertains to the idealized case of self-diffusivity within an individual cylindrical pore. How our results relate to real adsorptive materials, which are composed of networks of many pores, is an open question. Although outside the scope of this study, another open question is how the simple model for pore-averaged self-diffusivity presented in eqs 4−6 compares to more complex models (e.g., the friction based model of ref 25)? Another interesting question is how the introduction of surface roughness will impact the position-dependent dynamics. It seems obvious that the introduction of microscopic roughness will lead to slower axial self-diffusion in the film layer, but it is unclear if this in turn will affect interior self-diffusion. Another interesting question is how the position-dependent dynamics of mixtures behave. In the case of mixtures, fluid layers of different species can interact in interesting ways. For example, the first layer of one species may span several layers of another species. In this case, how do the layer-dependent dynamics relate to local structure? We intend to address many of these questions in future work.

■ ASSOCIATED CONTENT

Supporting Information

The Supporting Information is available free of charge on the ACS Publications website at DOI: 10.1021/acs.langmuir.7b03401.

Partition boundary identification, maximum value of density profile in the film layer, self-diffusivity of bulk fluid, position-dependent self-diffusivity analysis at additional pore sizes and using the ALL partitioning scheme, and comparison of model prediction and pore-averaged self-diffusivites at additional pore sizes (PDF)

■ AUTHOR INFORMATION

Corresponding Author

*E-mail: william.krekelberg@nist.gov.

ORCID

William P. Krekelberg: 0000-0002-2321-4584
Daniel W. Siderius: 0000-0002-6260-7727
Thomas M. Truskett: 0000-0002-6607-6468

Notes

The authors declare no competing financial interest.

■ ACKNOWLEDGMENTS

T.M.T. acknowledges support from the Welch Foundation (F-1696) and the National Science Foundation (1720595). J.R.E. acknowledge the financial support of the National Science Foundation (CHE-1362572).

■ REFERENCES

(1) Khoo, H. H.; Tan, R. B. H. Life cycle investigation of CO_2 recovery and sequestration. *Environ. Sci. Technol.* **2006**, *40*, 4016−4024.

(2) Morris, R. E.; Wheatley, P. S. Gas storage in nanoporous materials. *Angew. Chem., Int. Ed.* **2008**, *47*, 4966−4981.

(3) Li, J.-R.; Kuppler, R. J.; Zhou, H.-C. Selective gas adsorption and separation in metal-organic frameworks. *Chem. Soc. Rev.* **2009**, *38*, 1477−1504.

(4) Espinal, L.; Morreale, B. D. Materials challenges in carbon-mitigation technologies. *MRS Bull.* **2012**, *37*, 431−438.

(5) Li, J.; Y, M.; McCarthy, M. C.; Sculley, J.; Yu, J.; H, J.; Balbuena, P. B.; Zhou, H. Carbon dioxide capture-related gas adsorption and separation in metal-organic frameworks. *Coord. Chem. Rev.* **2011**, *255*, 1791−1823.

(6) Sing, K. S. W.; Everett, D. H.; Haul, R. A. W.; Moscou, L.; Pierotti, R. A.; Rouquerol, J.; Siemieniewska, T. Reporting physisorption data for gas/solid systems with special reference to the determination of surface area and porosity. *Pure Appl. Chem.* **1985**, *57*, 603−619.

(7) Gelb, L. D.; Gubbins, K. E.; Radhakrishnan, R.; Sliwinska-Bartkowiak, M. Phase separation in confined systems. *Rep. Prog. Phys.* **1999**, *62*, 1573−1659.

(8) Fan, C.; Do, D. D.; Nicholson, D. On the cavitation and pore blocking in slit-shaped ink-bottle pores. *Langmuir* **2011**, *27*, 3511−3526.

(9) Monson, P. A. Understanding adsorption/desorption hysteresis for fluids in mesoporous materials using simple molecular models and classical density functional theory. *Microporous Mesoporous Mater.* **2012**, *160*, 47−66.

(10) Thommes, M.; Kaneko, K.; Neimark, A. V.; Olivier, J. P.; Rodriguez-Reinoso, F.; Rouquerol, J.; Sing, K. S. W. Physisorption of gases, with special reference to the evaluation of surface area and pore size distribution (iupac technical report). *Pure Appl. Chem.* **2015**, *87*, 1051−1069.

DOI: 10.1021/acs.langmuir.7b03401
Langmuir 2017, 33, 13955−13963

(11) Keskin, S.; Liu, J.; Johnson, J. K.; Sholl, D. S. Testing the accuracy of correlations for multicomponent mass transport of adsorbed gases in metal-organic frameworks: Diffusion of h2/ch4 mixtures in cubtc. *Langmuir* **2008**, *24*, 8254−8261.
(12) Liu, J.; Keskin, S.; Sholl, D. S.; Johnson, J. K. Molecular simulations and theoretical predictions for adsorption and diffusion of CH4/H2 and CO2/CH4 mixtures in ZIFs. *J. Phys. Chem. C* **2011**, *115*, 12560−12566.
(13) Malek, K.; Sahimi, M. Molecular dynamics simulations of adsorption and diffusion of gases in silicon-carbide nanotubes. *J. Chem. Phys.* **2010**, *132*, 014310.
(14) Bhatia, S. K.; Nicholson, D. Anomalous transport in molecularly confined spaces. *J. Chem. Phys.* **2007**, *127*, 124701.
(15) Bonilla, M. R.; Bhatia, S. K. The low-density diffusion coefficient of soft-sphere fluids in nanopores: Accurate correlations from exact theory and criteria for applicability of the knudsen model. *J. Membr. Sci.* **2011**, *382*, 339−349.
(16) Bonilla, M. R.; Bhatia, S. K. Diffusion in pore networks: Effective self-diffusivity and the concept of tortuosity. *J. Phys. Chem. C* **2013**, *117*, 3343−3357.
(17) Frentrup, H.; Avendano, C.; Horsch, M.; Salih, A.; Müller, E. A. Transport diffusivities of fluids in nanopores by non-equilibrium molecular dynamics simulation. *Mol. Simul.* **2012**, *38*, 540−553.
(18) Zhu, F.; Tajkhorshid, E.; Schulten, K. Collective diffusion model for water permeation through microscopic channels. *Phys. Rev. Lett.* **2004**, *93*, 224501.
(19) Ravikovitch, P. I.; Neimark, A. V. Diffusion-controlled hysteresis. *Adsorption* **2005**, *11*, 265−270.
(20) Espinal, L.; Wong-Ng, W.; Kaduk, J. A.; Allen, A. J.; Snyder, C. R.; Chiu, C.; Siderius, D. W.; Li, L.; Cockayne, E.; Espinal, A. E.; Suib, S. L. Time-dependent CO_2 sorption hysteresis in a one-dimensional microporous octahedral molecular sieve. *J. Am. Chem. Soc.* **2012**, *134*, 7944−7951.
(21) Monson, P. A. Mean field kinetic theory for a lattice gas model of fluids confined in porous materials. *J. Chem. Phys.* **2008**, *128*, 084701.
(22) Naumov, S.; Khoklov, A.; Valiullin, R.; Karger, J.; Monson, P. A. Understanding capillary condensation and hysteresis in porous silicon: Network effects within independent pores. *Phys. Rev. E* **2008**, *78*, 060601.
(23) Monson, P. A. Fluids confined in porous materials: Towards a unified understanding of thermodynamics and dynamics. *Chem. Ing. Tech.* **2011**, *83*, 143−151.
(24) Edison, J. R.; Monson, P. A. Dynamic mean field theory of condensation and evaporation in model pore networks with variations in pore size. *Microporous Mesoporous Mater.* **2012**, *154*, 7−15.
(25) Bhatia, S. K.; Nicholson, D. Modeling self-diffusion of simple fluids in nanopores. *J. Phys. Chem. B* **2011**, *115*, 11700−11711.
(26) Bhatia, S. K.; Bonilla, M. R.; Nicholson, D. Molecular transport in nanopores: a theoretical perspective. *Phys. Chem. Chem. Phys.* **2011**, *13*, 15350.
(27) Mittal, J.; Truskett, T. M.; Errington, J. R.; Hummer, G. Layering and position-dependent diffusive dynamics of confined fluids. *Phys. Rev. Lett.* **2008**, *100*, 145901.
(28) Hinczewski, M.; von Hansen, Y.; Dzubiella, J.; Netz, R. R. How the diffusivity profile reduces the arbitrariness of protein folding free energies. *J. Chem. Phys.* **2010**, *132*, 245103.
(29) Carmer, J.; van Swol, F.; Truskett, T. M. Note: Position-dependent and pair diffusivity profiles from steady-state solutions of color reaction-counterdiffusion problems. *J. Chem. Phys.* **2014**, *141*, 046101.
(30) Bollinger, J. A.; Jain, A.; Carmer, J.; Truskett, T. M. Communication: Local structure-mobility relationships of confined fluids reverse upon supercooling. *J. Chem. Phys.* **2015**, *142*, 161102.
(31) Krekelberg, W. P.; Siderius, D. W.; Shen, V. K.; Truskett, T. M.; Errington, J. R. Connection between thermodynamics and dynamics of simple fluids in highly attractive pores. *Langmuir* **2013**, *29*, 14527−14535.
(32) Krekelberg, W. P.; Siderius, D. W.; Shen, V. K.; Truskett, T. M.; Errington, J. R. Connection between thermodynamics and dynamics of simple fluids in pores: Impact of fluid−fluid interaction range and fluid−solid interaction strength. *J. Phys. Chem. C* **2017**, *121*, 16316−16327.
(33) Siderius, D. W.; Gelb, L. D. Extension of the steele 10−4-3 potential for adsorption calculations in cylindrical, spherical, and other pore geometries. *J. Chem. Phys.* **2011**, *135*, 084703.
(34) NIST Standard Reference Simulation Website. 2017; http://doi.org/10.18434/T4M88Q, NIST Standard Reference Database 173; accessed May, 2017.
(35) Liu, P.; Harder, E.; Berne, B. J. On the calculation of diffusion coefficients in confined fluids and interfaces with an application to the liquid−vapor interface of water. *J. Phys. Chem. B* **2004**, *108*, 6595−6602.
(36) Barker, J. A.; Henderson, D. Perturbation theory and equation of state for fluids. II. a successful theory of liquids. *J. Chem. Phys.* **1967**, *47*, 4714−4721.
(37) Mittal, J.; Errington, J. R.; Truskett, T. M. Thermodynamics predicts how confinement modifies the dynamics of the equilibrium hard-sphere fluid. *Phys. Rev. Lett.* **2006**, *96*, 177804.

DOI: 10.1021/acs.langmuir.7b03401
Langmuir 2017, 33, 13955−13963